Ceramics International 49 (2023) 22736–22744

Contents lists available at ScienceDirect

Ceramics International

journal homepage: www.elsevier.com/locate/ceramint

Comparative study on protective Cr coatings on nuclear fuel cladding Zirlo substrates by AIP and HiPIMS techniques

Zheng Wang [a,b], Wentao Li [a,b], Zhenyu Wang [a,b], Ming Li [a,c], Aiying Wang [a,b], Peiling Ke [a,b,*]

[a] Key Laboratory of Marine Materials and Related Technologies, Zhejiang Key Laboratory of Marine Materials and Protective Technologies, Ningbo Institute of Materials Technology and Engineering, Chinese Academy of Sciences, Ningbo, 315201, China
[b] Center of Materials Science and Optoelectronics Engineering, University of Chinese Academy of Sciences, Beijing, 100049, China
[c] Ningbo New Material Testing and Evaluation Center Co. Ltd, Ningbo, 315048, China

ARTICLE INFO

Handling Editor: P. Vincenzini

Keywords:
Cr coatings
Oxidation resistance
ATFs cladding
HiPIMS
AIP

ABSTRACT

After the Fukushima nuclear accident, the concept of accident-tolerant fuel (ATF) cladding coating was proposed with the aim of increasing the rescue time in the case of an accident. Cr coatings are considered to be promising ATFs cladding materials for loss-of-coolant-accident conditions. The oxidation behavior of a Cr coating is dominated by the microstructure and defects formed during the deposition process. To endow the Cr coatings with excellent oxidation resistance under a high-temperature steam environment, we deposited Cr coatings on Zirlo substrates by high-impulse-power magnetron sputtering (HiPIMS), a technique that can optimize the microstructure of the coating compared to the traditional arc ion plating (AIP) technique. The results revealed that the HiPIMS-Cr coatings exhibited a better steam oxidation resistance, and their oxidation weight gains were 14.6% and 42.4% lower than those of AIP-Cr coatings at 1100 °C and 1200 °C, respectively.

1. Introduction

Due to their low thermal neutron absorption cross-section, superior mechanical properties and good corrosion resistance under harsh irradiation conditions, zirconium alloys such as Zircaloy-4 [1–3] and Zirlo [4] have been extensively used as fuel cladding materials in light water reactors (LWRs) to separate the core fuels and cooling water during high-temperature operation. However, once the reaction between zirconium and steam is triggered at high temperatures, the release of a large amount of hydrogen gas leads to severe damage from loss-of-coolant accidents (LOCA), such as the Fukushima nuclear accident. Alternatively, surface protective coatings are considered as one of the most promising strategies with higher reliable as well as lower cost to improve the safety of accident tolerant fuels (ATFs), which can suppress the vital reaction between steam and zirconium and subsequently delay or even avoid LOCA disasters.

In recent years, considerable efforts have been exerted to prepare ATF cladding coatings with controllable properties, including SiC coatings [5], Cr coatings [2,3,6] FeCrAl coatings [1,7], and MAX phase coatings [8,9]. Among these coatings, both FeCrAl and SiC coatings display excellent oxidation resistance at high temperatures, but the former suffers from strong performance deterioration arising from the interfacial diffusion of Fe and Zr atoms [1], while the latter is prone to become worn out due to the extreme brittleness of ceramics. MAX phases [10–13] are known as a novel family of nano-laminated ternary carbides or nitrides with hexagonal crystal structures, where M represents an early metal element, A represents an A-group element mainly from the IIIA and IVA groups, and X is either carbon or nitrogen. This unique structure endows the MAX phase coatings with the combined physicochemical advantages of metals and ceramics for high-temperature and neutron activation. However, fabrication of a MAX phase coating with high purity and low deposition temperature is still an open challenge due to the composition complexities and narrow phase-formation limitations [14]. Compared to other coatings, Cr coatings deposited by laser beam, spraying, or physical vapor deposition (PVD) methods exhibit superior protective performance under both normal and accident conditions in reactors [1,2,6]. In addition, Cr coatings prepared by PVD technique possess much denser structure, which is vital for its ability to protect zirconium substrate from corrosion against high-temperature steam, compared to those synthesized by laser beam and spraying techniques.

In the development of vacuum-deposited Cr technology for ATFs, the

* Corresponding author. Key Laboratory of Marine Materials and Related Technologies, Zhejiang Key Laboratory of Marine Materials and Protective Technologies, Ningbo Institute of Materials Technology and Engineering, Chinese Academy of Sciences, Ningbo, 315201, China.
E-mail address: kepl@nimte.ac.cn (P. Ke).

https://doi.org/10.1016/j.ceramint.2023.04.074
Received 2 February 2023; Received in revised form 16 March 2023; Accepted 10 April 2023
Available online 19 April 2023

optimization of the PVD method based on the plasma charge theory is mainly assigned to direct current magnetron sputtering (dc-MS), arc ion plating (AIP), and high-impulse-power magnetron sputtering (HiPIMS). Han et al. found that the Cr coating deposited by dc-MS exhibited excellent oxidation resistance under a steam environment when oxidized at 1000–1200 °C due to the formation of a dense and adherent Cr_2O_3 layer on the coating surface [3]. Nevertheless, the Cr coating obtained by dc-MS deposition has been reported to exhibit poor protective characteristics due to the presence of a large columnar crystal structure in the coating [2]. Compared to the traditional dc-MS, the AIP method based on vacuum arc evaporation shows an increased metal ionization rate during plasma discharge that can favor dense and uniform Cr coatings that strongly adhere to the zirconium alloy substrate. However, the AIP technique has the drawback of the synergistic deposition of macro-particles and the formation of micro-pinholes in the coating that stimulate the penetration of corrosive media and the deterioration of protective functions. Another alternative to the PVD method is the recently developed HiPIMS. HiPIMS shows the combined advantages of a higher ionization fraction of metal atoms than that of dc-MS and a smoother dense structure without macroparticles in the coating compared to that of AIP [15,16]. Therefore, it can be expected that the novel HiPIMS [17–19] approach endows the Cr coating with sufficient capability for use as a protective layer in technological LOCA applications. The dependence of HiPIMS process upon oxidation behavior of Cr coating is far lack of study for nuclear fuel cladding Zirconium alloys, although much attention has been devoted onto the progress of electrochemical and decorative hard coatings.

The Cr coatings deposited by PVD method usually exhibit significant columnar crystal structure. In addition, the refined columnar crystals are more beneficial to form a compact oxide scale, which can effectively hinder the penetration of external corrosive medium. In this study, two differently structured Cr coatings were prepared. One is a fine-grained HiPIMS-Cr and the other is a coarse-grained AIP-Cr. The steam oxidation resistance of the coatings at the temperatures ranging from 1100 to 1200 °C was investigated for comparison. Furthermore, the failure mechanism of the two Cr coatings was discussed based on the differences in microstructural morphologies, crystalline phase orientation and oxidation behaviors.

2. Experimental procedure

Zirlo alloys with dimensions of 15 mm × 10 mm × 2 mm were used as the substrates. The weight percentages of the major alloying elements were Sn, 1.0%; Nb, 1.0%; Fe, 0.1%; and balance Zr. Prior to deposition, the substrates were first polished to 3000-grit using silicon carbon paper and then were ultrasonically cleaned in acetone and ethanol for 15 min each. For comparison, Cr coatings were deposited on Zirlo substrates with homemade HiPIMS and AIP systems (Fig. 1). Detailed descriptions of the two devices can be found in our previous works [15,20].

During the deposition process, the substrates were hung on the rotated jig plate facing the magnetron sputtering target and the AIP target to enhance the coating uniformity. The chamber was pumped down to a base pressure lower than 2.8×10^{-5} Torr and heated to 200 °C. Argon gas was introduced to a linear ion beam source, where Ar^+ ion precleaning was generated at a bias of −600 V to remove the contamination or oxides adherent to the substrate surface. During all depositions, a DC-pulsed negative bias of −80 V was applied to the substrate for the HiPIMS and AIP processes. The deposit time was controlled to obtain similar coating thicknesses for each deposition method. The parameters used for the deposition with the two techniques are listed in Table 1.

For the Cr coatings deposited by the two different methods, high-temperature steam oxidation tests were conducted in a thermogravimetric analyzer (TGA, SETARAM SETSYS, France). In particular, the coated samples were exposed to water vapor at 50% relative humidity (RH) at 1100 °C and 1200 °C for different times. During the measurements, the samples were heated from 40 °C to the designated temperatures at a rate of 50 °C/min. High-temperature steam was supplied to the oxidation chamber during the heating procedure. The cross-section and surface morphology of the specimens were characterized using a scanning electron microscope (SEM, FEI Quanta FEG 250) equipped with an energy dispersive X-ray spectrometer (EDS, Oxford X-Max). An electron backscattered diffraction (EBSD) test was performed using an SEM (Verios G4 UC) in order to investigate the microstructure evolution. The crystal structures of the specimens were analyzed by X-ray diffraction (XRD) using a Bruker D8 Advance diffractometer (Bruker, Germany) with Cu K_α radiation. In addition, the cross-sectional EBSD and SEM samples were grinded with SiC grinding papers down to 3000 grit, then followed by Ar-ion milling and mechanical polishing, respectively. The steam oxidized cross-section samples were etched for 10 s in 1.0% HF+1.5% HCl +2.5% HNO_3+95% H_2O mixed acid and observed by SEM.

3. Results and discussion

3.1. Structure and composition of coating

Fig. 2 shows the difference in the surface morphology of the Cr coatings prepared by HiPIMS and AIP. It is clearly observed that the surface morphology of the coatings varies significantly due to the different preparation methods. As shown in Fig. 2(a) and (c), the HiPIMS-Cr coating exhibited a compact structure and smooth surface free of macroparticles. This surface morphology can be attributed to the high metal ionization of Cr atoms and plasma density during deposition that are almost two or three orders of magnitude higher than those of the traditional dc-MS techniques [16,21]. In addition, a relatively dense microstructure was still observed on the surface of the AIP-Cr coating (Fig. 2(b) and (d)). This was because the AIP technique also exhibits a high metal ionization rate. However, noted that different from the smooth surface of HiPIMS-Cr coating, many large macro-particles emerged on the surface of AIP-Cr coating because of the arc spot evaporation, where the liquid droplets from Cr target were always ejected

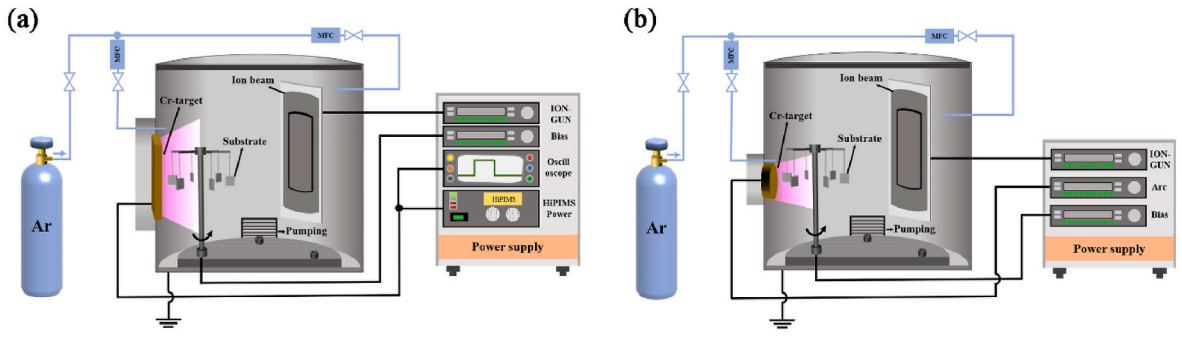

Fig. 1. Schematics of (a) HiPIMS-Cr and (b) AIP-Cr coating deposition systems.

Table 1
Deposition parameters of the HiPIMS-Cr and AIP-Cr coatings.

Method	Time (min)	Ar flow (sccm)	Pressure (mTorr)	Bias voltage (-V)	Power supply				
					Power (kW)	Current (A)	Voltage (V)	Pulse width (μs)	Duty ratio
Etching	15	40	2.5	600	–	–	–	–	–
HiPIMS	500	50	1.8	80	3.0	4.0	760	100	5%
AIP	900	50	1.8	80	1.2	70	17	–	100%

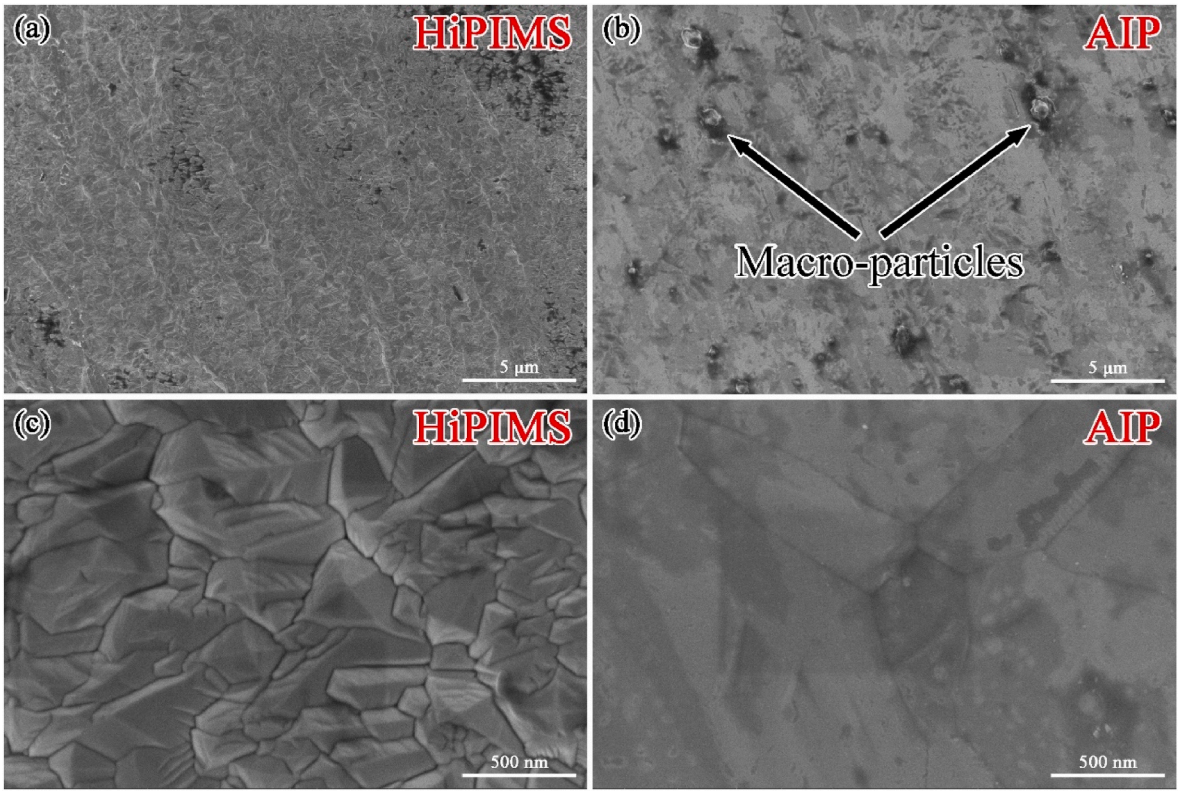

Fig. 2. Surface SEM images of the Cr coatings. (a) and (b) show the images for the HiPIMS-Cr and AIP-Cr coatings, respectively. (c) and (d) show the corresponding images at high magnification.

during plasma discharge of AIP process.

Fig. 3 shows the cross-section morphology and corresponding EBSD patterns of the Cr coatings deposited by different techniques. Although the deposition power was controlled in various processes, Fig. 3(a) and (b) illustrate that the thickness of the HiPIMS-Cr and AIP-Cr coatings were 12.14 μm and 11.22 μm, respectively. This slight difference in the thickness was attributed to the different deposition rates. Because the crystallography details cannot be obtained from the SEM morphology observation, the EBSD test was performed to reveal the grain characteristics for different Cr coatings. As shown in Fig. 3(c) and (d), the HiPIMS-Cr coating exhibited refined dense and uniform columnar crystals, with the mean columnar size much smaller than that of the AIP-Cr coating. In particular, very coarse columnar crystals with a maximum columnar diameter of 1.68 μm were observed for the AIP-Cr coating. Indeed, both HiPIMS and AIP had a similar high mental ionization, useful to the enhanced compactness in the coating structure. It should note that HiPIMS technique with a high plasma density and a relative low ion energy can promote grain refinement, while the AIP technique had a high plasma density and high ion energy [22]. In addition, these results were consistent with the structural variety of the HiPIMS-Cr and AIP-Cr coatings shown in Fig. 2(c) and (d).

Fig. 4 shows the XRD patterns of the Cr coatings prepared by the HiPIMS and AIP techniques. Both the XRD spectra of the as-deposited HiPIMS-Cr and AIP-Cr coatings were mainly composed of three peaks located at 44°, 64° and 82°, corresponding to the diffraction signals of the (110), (200) and (211) orientations, respectively. Moreover, the two coatings showed different crystallographic orientation. The (110)-preferred orientation was assigned to HiPIMS-Cr coating, while the (200)-preferred orientation was assigned to AIP-Cr coating. To quantitatively identify the preferred orientation of Cr coatings, the texture coefficients of the as-deposited coatings at various crystal planes were calculated using the following formulas [23]:

$$TC = \frac{I(hkl)/I_0(hkl)}{(1/n)\sum[I(hkl)/I_0(hkl)]} \quad (1)$$

where n is the number of diffraction peaks and I_0 and I are the intensity of the diffraction peak in the standard PDF card of the crystal plane and the actual intensity of the diffraction peak of the crystal plane, respectively.

Table 2 lists the calculation results of the specific texture coefficients of the two Cr coatings. Generally, larger values of the texture coefficients correspond to the strongly preferred phase orientation in the crystal. According to the coating growth mechanism during PVD deposition, the close-packed (110) orientation generally has the lowest surface energy compared to the (200) and (211) textures. However, interestingly, it was found that the HiPIMS-Cr coating exhibited (110)-preferred orientation and the AIP-Cr coating exhibited (200)-preferred orientation, and a

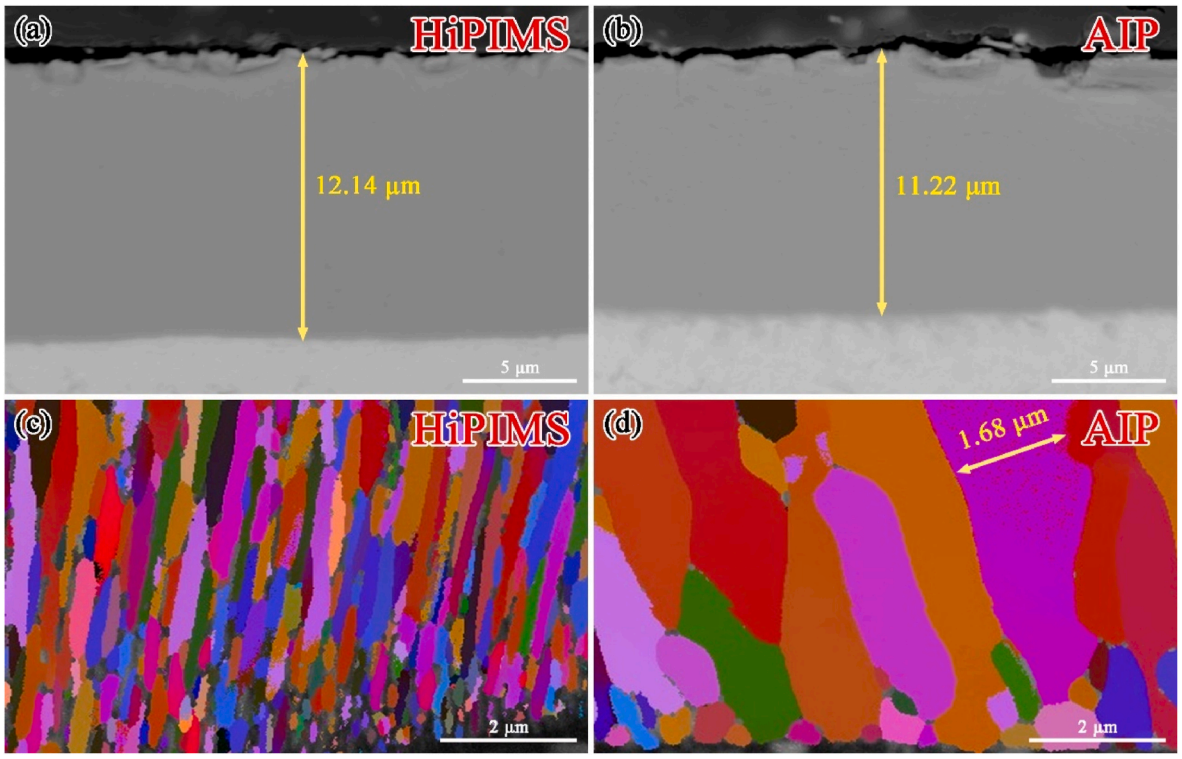

Fig. 3. Cross-section SEM images of Cr coatings. (a) and (b) show the images for the HiPIMS-Cr and AIP-Cr coatings, respectively. (c) and (d) are the corresponding EBSD Euler images.

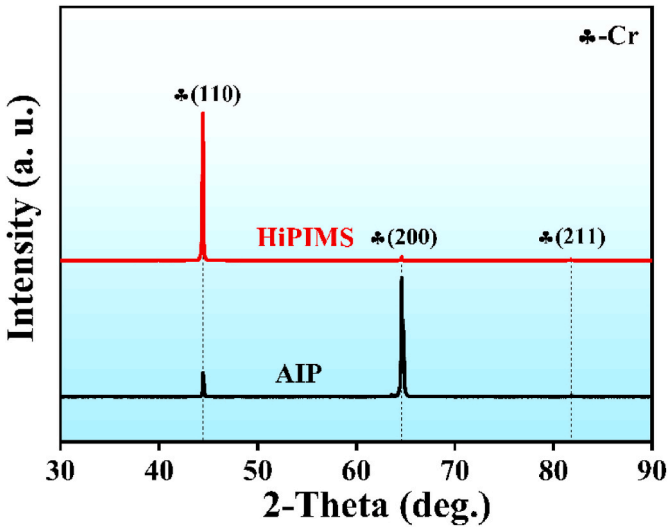

Fig. 4. X-ray diffraction patterns of HiPIMS-Cr and AIP-Cr coatings.

Table 2
Texture coefficients of the HiPIMS-Cr and AIP-Cr coatings.

Preparation method	(110) texture	(200) texture	(211) texture
HiPIMS	2.443	0.415	0.142
AIP	0.035	2.950	0.015

higher texture coefficient for the (110) crystal plane was observed for the HiPIMS-Cr coating at 2.443 than that of the AIP-Cr coating at 0.035. In contrast to dc-MS and HiPIMS, the AIP technique exhibited higher plasma energy, enhancing the diffusion capacity of the absorbed atoms along the surface, and subsequently led to the formation of an intense (200)-preferred orientation. Compared to AIP, the HiPIMS technique has a relatively lower plasma energy, enhancing the possibility of forming a (110) orientation during the nucleation process. Meng et al. [24] reported that Cr coatings with a strong (110) texture exhibit a better steam oxidation resistance at high temperatures than those with a strong (200) texture. Hence, it is expected that HiPIMS-Cr coating perform better in high-temperature steam environment.

3.2. Oxidation at 1100–1200 °C

Fig. 5 shows the surface SEM images of the HiPIMS-Cr and AIP-Cr coatings oxidized at 1100 °C for 90 min. After oxidation, white floc-like oxides appeared on the surface of the two Cr coatings. When EDS was used to analyze their chemical element composition, it was found that the white flocs were enriched in O (see Table 3). Yeom et al. [25] reported that the growth of the white flocs was driven by the rapid diffusion of Cr cations across their own metal oxide layer through short-circuit paths. In particular, a large number of white flocs were distributed on the surface of the AIP-Cr coating and the amount of these oxides in the AIP-Cr coating was significantly higher than that in the HiPIMS-Cr coating. The number of white flocs was related to the grain size and the number of defects in the Cr coatings. The oxides of Cr coatings with coarser grain size easily spalled off during cooling. In addition, the macro-particles destroyed the integrity of the coatings. As a result, a large number of white flocs formed in the site of macro-particles with the oxidation process.

Fig. 6 displays the cross-sectional morphologies of the bare Zirlo substrate and the HiPIMS-Cr and AIP-Cr coatings after oxidation at 1100 °C for 90 min. As shown in Fig. 6(a), a ZrO_2 oxide scale with a thickness of 94.6 μm was clearly formed on the surface of the bare Zirlo substrate, where many defects appeared due to the occurrence of "breakaway" oxidation phenomena [26]. However, the Cr coatings prepared by both the AIP and HiPIMS technologies demonstrated excellent protective properties after the steam test for the Zirlo substrate. As shown in Fig. 6(b) and (c), even though different oxidation

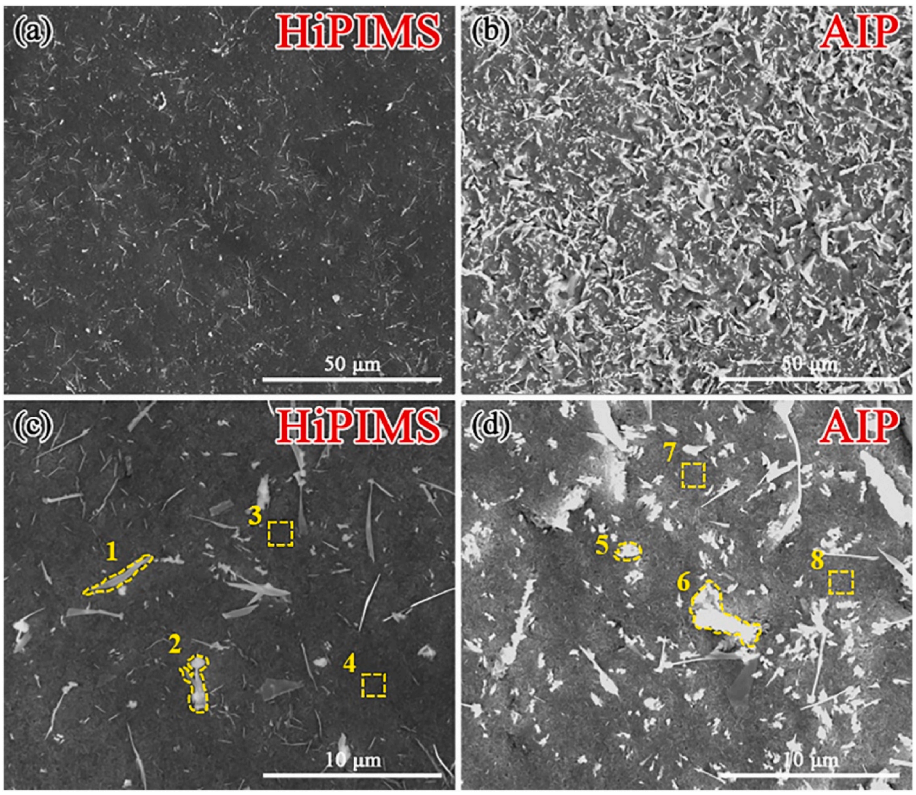

Fig. 5. Surface SEM images of the Cr coatings oxidized at 1100 °C for 90 min. (a) and (b) show the images for the HiPIMS-Cr and AIP-Cr coatings, respectively. (c) and (d) show the corresponding images at high magnification.

Table 3
Chemical compositions of the EDS point analysis in Fig. 5.

At.%	HiPIMS-Cr				AIP-Cr			
	1	2	3	4	5	6	7	8
Cr	35.94	36.11	39.37	40.01	35.66	34.85	40.02	40.98
O	64.06	63.89	60.63	59.99	64.34	65.15	59.98	59.02

damage of the coatings occurred during harsh steam test, the thicknesses of the residual Cr coatings deposited by HiPIMS and AIP were still approximately 7.5 μm and 5.2 μm, respectively. As for the two Cr coatings with BCC lattices, the close-packed (110) orientation had the highest reticular density compared to the (200) and (211) textures. So, the HiPIMS-Cr coating with intense (110) texture can hinder the permeation of outside oxygen more efficiently and protect the substrate much better. Moreover, the HiPIMS-Cr coating exhibited fewer oxide/-metal interface voids compared with AIP-Cr coating after oxidation. This was because numerous GBs (grain boundaries) in the HiPIMS-Cr coating annihilated the cation vacancies from the oxide scale and the

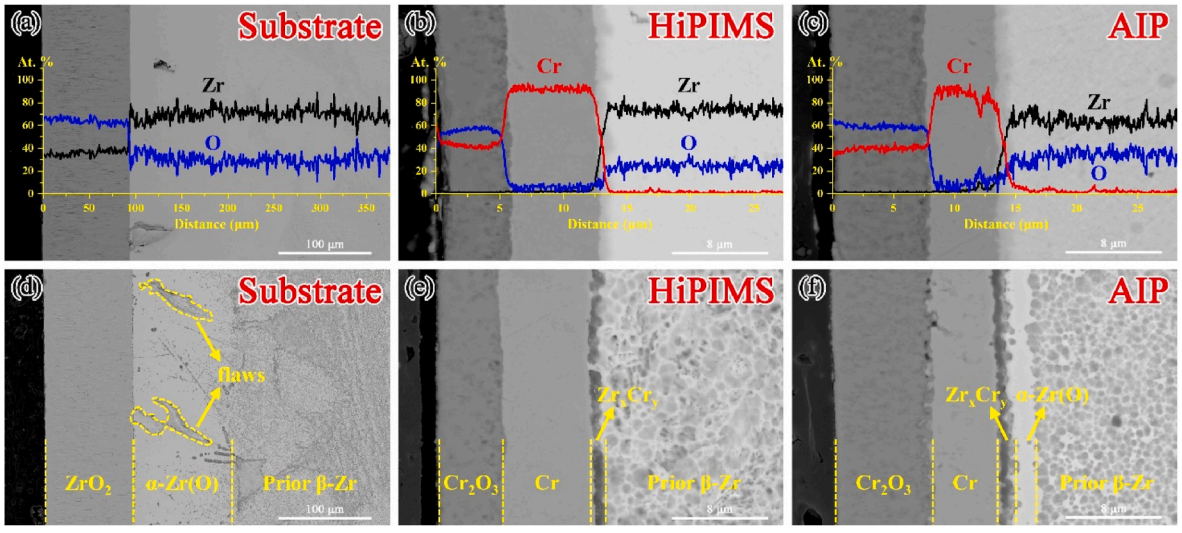

Fig. 6. Cross-section SEM images of the bare Zirlo substrate (a) and the Cr-coated Zirlo substrates (b, c) oxidized at 1100 °C for 90 min with the corresponding EDS results. (d–f) Show the corresponding cross-section images after chemical corrosion.

"Kirkendall" vacancies from the residual metal layer during oxidation [27,28]. In addition, a Zr_xCr_y transition layer was formed owing to the diffusion of element at the interface of prepared Cr coatings and Zirlo substrates.

In fact, the steam will react with β-Zr to form a superficial layer of ZrO_2 oxide scale and an intermediate layer of oxygen-stabilized α-Zr(O) at high temperatures [29]. For further evaluated the oxygen permeation resistance of substrate and the two Cr coatings, corresponding cross-section SEM was also performed after high-temperature oxidation and chemical corrosion, as shown in Fig. 6(d–f). The α-Zr(O) layer thicknesses of bare Zirlo substrate and AIP-Cr coating were 110.8 μm and 2.3 μm, respectively, while the HiPIMS-Cr coating did not show obvious α-Zr(O) layer. Considering that the as-deposited thickness was 12.14 μm and 11.22 μm for the HiPIMS-Cr and AIP-Cr coatings before the steam test, respectively, the HiPIMS-Cr coating showed a better oxidation resistance than the AIP-Cr coating under the high-temperature steam environment.

Although the oxidation behavior of the coatings could be identified to some extent by the microstructure of the coatings after oxidation, it was difficult to visually reflect the oxidation process of the coatings. To further compare the steam oxidation resistance of the HiPIMS-Cr and AIP-Cr coatings at high temperatures, we obtained the oxidation kinetics curves of the bare Zirlo substrate and the HiPIMS-Cr and AIP-Cr coatings at 1100 °C for 90 min, as shown in Fig. 7. As shown in Fig. 7(a), the Zirlo substrate exhibited a high oxidation rate, and the oxidation weight gain of the Zirlo substrate was significantly larger than those of the HiPIMS-Cr and AIP-Cr coatings. Fig. 7(b) shows the relationship between the square of the oxidation weight gain ($\triangle W^2$) of the Zirlo substrate and the oxidation time. The $\triangle W^2$ of the Zirlo substrate showed a linear dependence on the oxidation time, indicating that its oxidation kinetics obeyed a parabolic law [30], and the rate-determining step was diffusion-controlled. However, the oxidation weight gains of the two Cr coatings after oxidation were small. As shown in Fig. 7(c), the oxidation process can be divided into two stages. Stage I was the heating process and stage II was the oxidation process at 1100 °C for 90 min. In addition, the HiPIMS-Cr and AIP-Cr coatings also presented a parabolic oxidation law, with the parabolic rate constants of 6.87×10^{-6} g^2/cm^4•min and 9.12×10^{-6} g^2/cm^4•min, respectively. Therefore, based on the oxidation kinetics results, the HiPIMS-Cr coating exhibited a better steam oxidation resistance than the AIP-Cr coating at 1100 °C.

Considering the excellent oxidation resistance of Cr coatings under a high-temperature steam environment, the anti-oxidation behaviors of the HiPIMS-Cr and AIP-Cr coatings after steam oxidation at 1200 °C for 90 min were further compared and evaluated. As the oxidation temperature was increased to 1200 °C, some white flocs still appeared on the surfaces of the HiPIMS-Cr and AIP-Cr coatings. However, the surface of HiPIMS-Cr and AIP-Cr coatings exhibited extremely different structure after oxidation at 1200 °C. As shown in Fig. 8(d), clear microcracks were observed on the surface of the AIP-Cr coating, and the formed oxides exhibited a loose structure. In addition, a large number of bubbles were distributed on the surface of HiPIMS-Cr coating, as shown in Fig. 8(a) and (c), and these bubbles were connected in a network. Wei et al. [31] reported that the evaporation of gaseous CrO_3 may have resulted in forming bubbles. The number of microcracks and bubbles may be related to the grain size and the number of defects in the Cr coatings. Compared to the AIP-Cr coating, the HiPIMS-Cr coating exhibited dense and smooth surface with refined columnar crystals, which was in favor of the formation of compact oxide scale under a high-temperature steam environment, and therefore hindered the initiation of microcracks. The results showed that the HiPIMS-Cr coating still had relatively excellent oxidation resistance under a 1200 °C steam environment, even though a coarse network of bubbles appeared on its surface.

Fig. 9 shows the difference in the cross-sectional morphology for the Cr coatings prepared by HiPIMS and AIP after oxidation at 1200 °C for 90 min. Compared to oxidation at 1100 °C, the oxide scale thicknesses of the HiPIMS-Cr and AIP-Cr coatings decreased at different degrees after

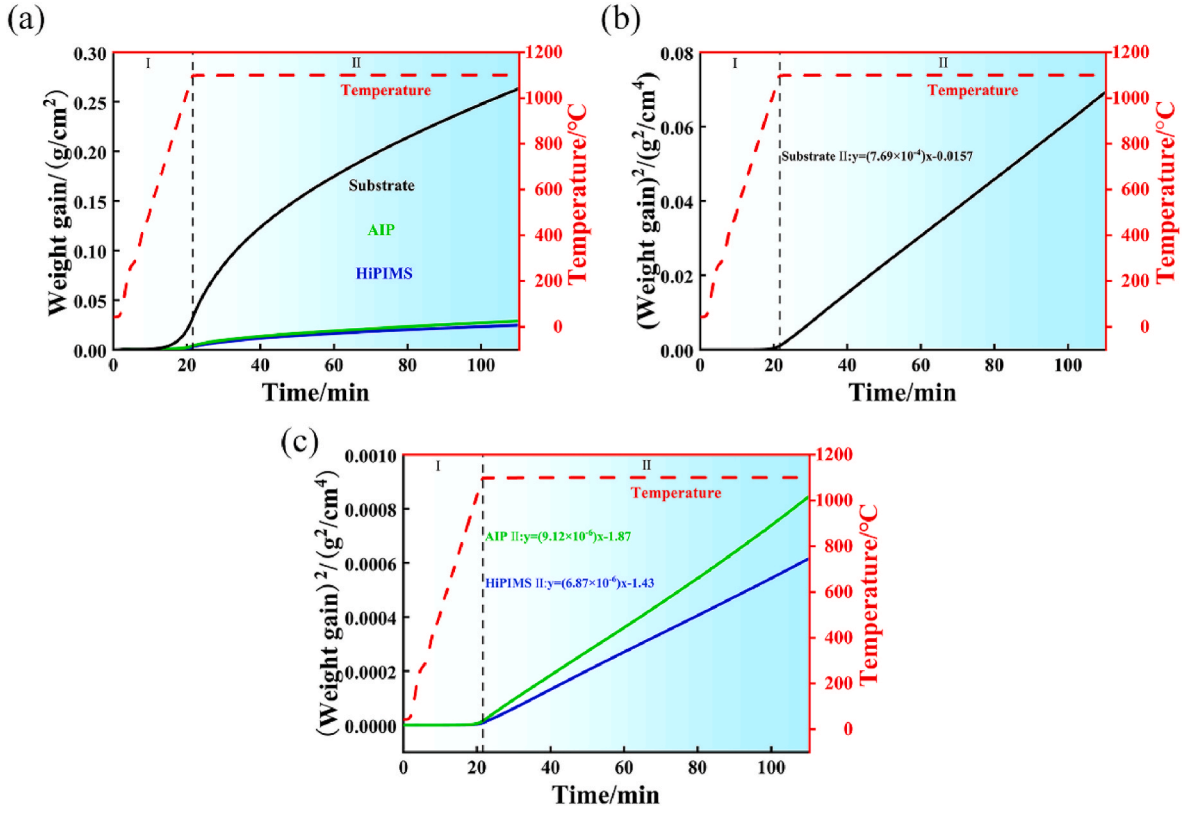

Fig. 7. Oxidation kinetics curves of the Zirlo substrate and two kinds of Cr coatings in 1100 °C steam environment. (a) Shows the change in the oxidation weight gain with oxidation time. (b) and (c) show the changes of the square of the oxidation weight gain with oxidation time.

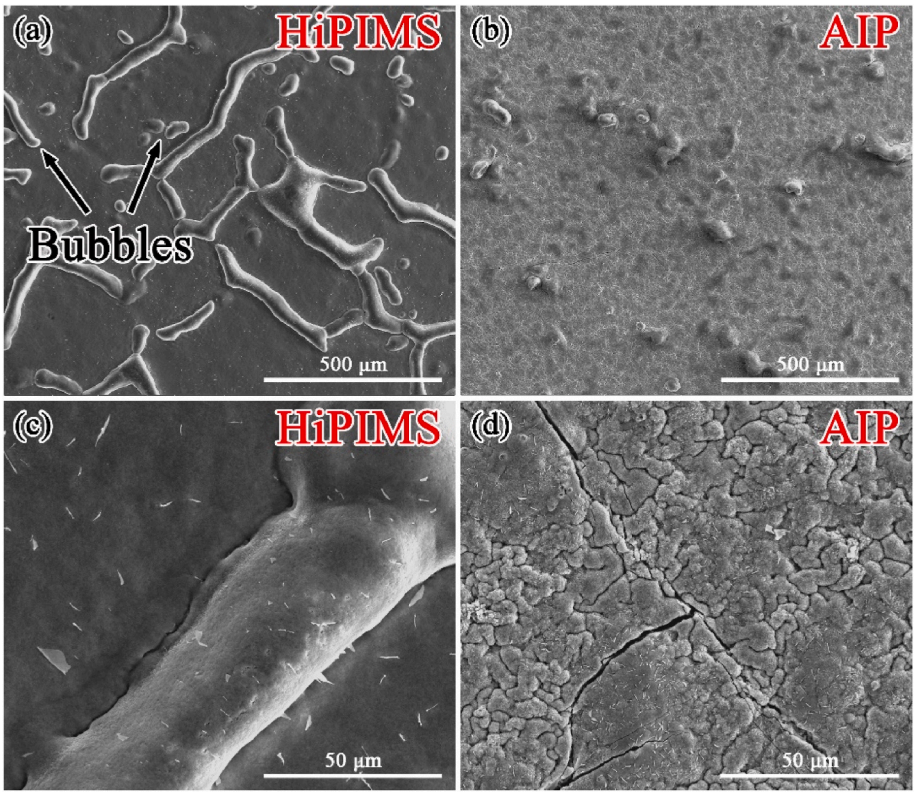

Fig. 8. Surface SEM images of the Cr coatings oxidized at 1200 °C for 90 min. (a) and (b) show the images for the HiPIMS-Cr and AIP-Cr coating, respectively. (c) and (d) show the corresponding images at high magnification.

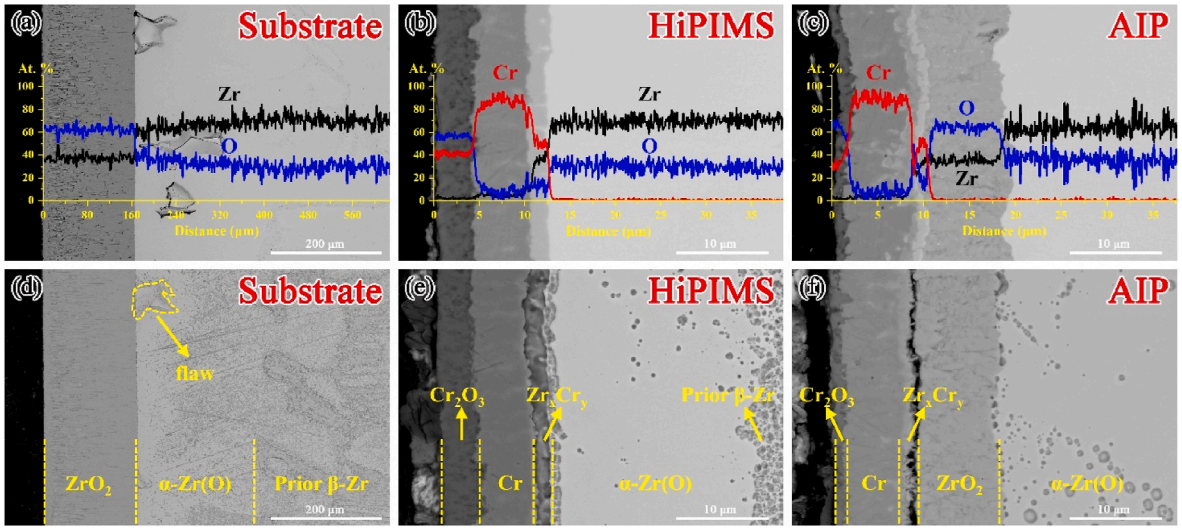

Fig. 9. Cross-section SEM images of the bare Zirlo substrate (a) and the Cr-coated Zirlo substrates (b, c) oxidized at 1200 °C for 90 min with the corresponding EDS results. (d–f) Show the corresponding cross-section images after chemical corrosion.

oxidation at 1200 °C. One important reason for this was that the Cr_2O_3 was reduced by the Zirlo substrate when the thickness of Cr_2O_3 reached its maximum [19]. Another key factor was the difference of oxide scale structure generated by the grain size and macroparticles. For the AIP-Cr coatings oxidized at 1200 °C for 90 min, as shown in Fig. 9(c) and (f), the relatively loose oxide scale could not effectively prevent the permeation of outside oxygen. As a result, the residual AIP-Cr coating was consumed rapidly, followed by a reduced metallic Cr layer and a ZrO_2 layer generated below the Cr_2O_3 oxide scale. On the contrary, a compact oxide scale formed on the surface of HiPIMS-Cr coating, which played a role in hindering oxygen diffusion and postponing the chemical reaction between Zirlo substrate and Cr_2O_3. These results further proved that the HiPIMS-Cr coating exhibited more excellent steam oxidation resistance than the AIP-Cr coating at high temperatures.

Fig. 10 shows the oxidation kinetics curves of the bare Zirlo substrate and the HiPIMS-Cr and AIP-Cr coatings at 1200 °C for 90 min. Compared to oxidation at 1100 °C, the oxidation kinetics curve of the bare Zirlo substrate (Fig. 10(b)) still obeyed a parabolic law, with the parabolic rate constant increased from 7.69×10^{-4} $g^2/cm^4 \bullet min$ to 3.63×10^{-3} $g^2/cm^4 \bullet min$. However, the oxidation kinetics curve of the HiPIMS-Cr

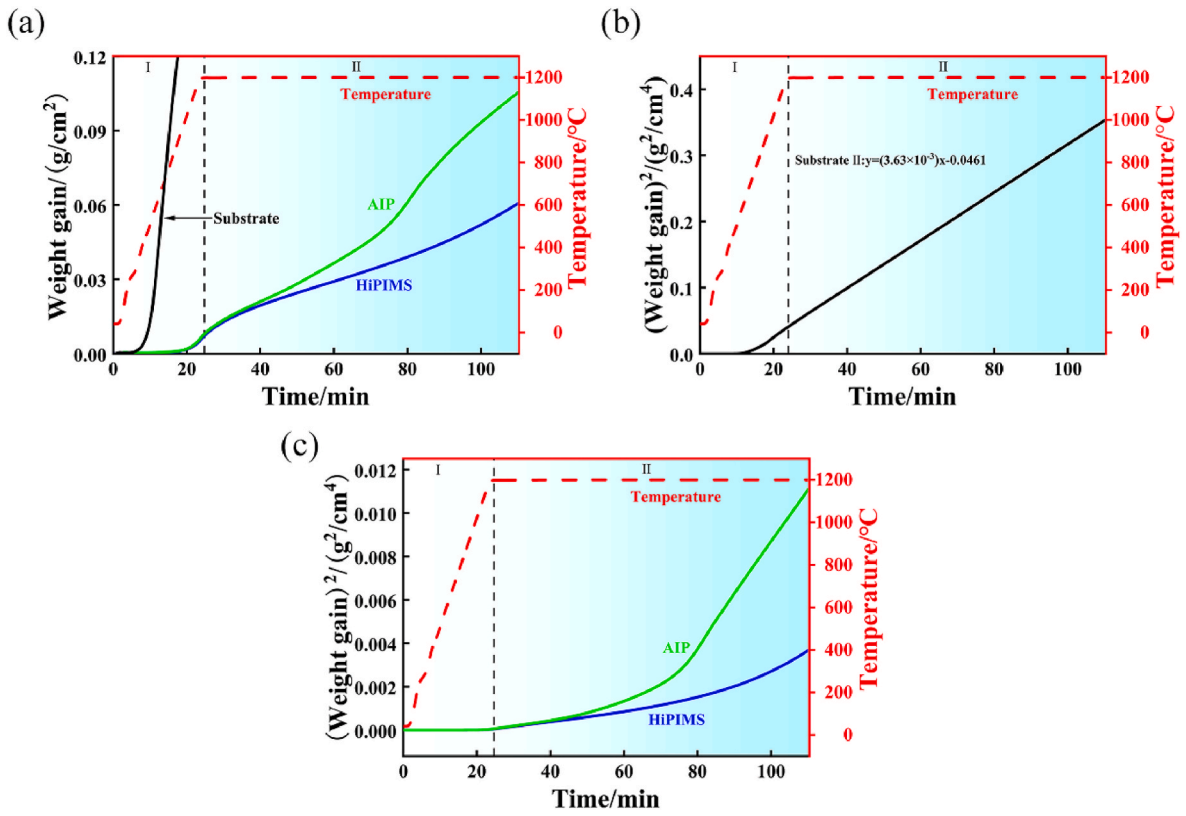

Fig. 10. Oxidation kinetics curves of the Zirlo substrate and two kinds of Cr coatings in 1200 °C steam environment. (a) Shows the change in the oxidation weight gain with oxidation time. (b) and (c) show the changes of the square of the oxidation weight gain with oxidation time.

and AIP-Cr coatings (Fig. 10(c)) did not obey the parabolic law in 1200 °C steam environment. Yeom [25] pointed out that this phenomenon was attributed in part to the volatilization of Cr species at the higher temperature. Combined with the structure analysis of oxide scale, it can be concluded that the volatilization of Cr species was reduced in the HiPIMS-Cr coating. In addition, compared with the Zirlo substrate, the oxidation weight gain of the HiPIMS-Cr and AIP-Cr coatings were decreased 89.8% and 82.3%, respectively. Therefore, the HiPIMS-Cr coating was provided with excellent high-temperature oxidation resistance and can improve the safety of ATF zirconium cladding significantly to reduce its rate of oxidation weight gain greatly.

4. Conclusions

In this study, we fabricated Cr coatings on Zirlo substrates using two different techniques, HiPIMS and AIP. The steam oxidation resistance of the coatings was comparatively studied in the temperature range of 1100–1200 °C. Compared to the AIP-Cr coating, the HiPIMS-Cr coating exhibited a better steam oxidation resistance at high temperatures, which could be attributed to the difference in microstructure and defects formed during deposition. Due to the coarse columnar crystal structure with macroparticles on the surface, the AIP-Cr coating exhibited loose oxide scale and relatively poor steam oxidation resistance. On the contrary, because of the dense and smooth surface with refined columnar crystals, a compact oxide scale was formed on the surface of HiPIMS-Cr coating, which played an important role in hindering the permeation of outside oxygen and the corrosion of Zirlo substrate. Besides, the HiPIMS-Cr coating exhibited a relatively higher (110) texture intensity than the AIP-Cr coating. This may be another important reason for the better steam oxidation resistance of the HiPIMS-Cr coating at high temperatures. This work provides reference information and guidance for the preparation of Cr coatings on the surfaces of nuclear cladding tubes in the future.

Declaration of competing interest

The authors declare that they have no known competing financial interests or personal relationships that could have appeared to influence the work reported in this paper.

Acknowledgements

This research was supported by the CAS Interdisciplinary Innovation Team (292020000008), National Natural Science Foundation of China (52025014), Key Research and Development Program of Ningbo (20232ZDYF020062) and Youth Innovation Promotion Association CAS (2023312).

References

[1] X.C. Han, Y. Wang, S.M. Peng, H.B. Zhang, Oxidation behavior of FeCrAl coated Zry-4 under high temperature steam environment, Corrosion Sci. 149 (2019) 45–53, https://doi.org/10.1016/j.corsci.2019.01.004.
[2] J.C. Brachet, I. Idarraga-Trujillo, M. Le Flem, M. Le Saux, V. Vandenberghe, S. Urvoy, E. Rouesne, T. Guilbert, C. Toffolon-Masclet, M. Tupin, C. Phalippou, F. Lomello, F. Schuster, A. Billard, G. Velisa, C. Ducros, F. Sanchette, Early studies on Cr-Coated Zircaloy-4 as enhanced accident tolerant nuclear fuel claddings for light water reactors, J. Nucl. Mater. 517 (2019) 268–285, https://doi.org/10.1016/j.jnucmat.2019.02.018.
[3] X.C. Han, J.X. Xue, S.M. Peng, H.B. Zhang, An interesting oxidation phenomenon of Cr coatings on Zry-4 substrates in high temperature steam environment, Corrosion Sci. 156 (2019) 117–124, https://doi.org/10.1016/j.corsci.2019.05.017.
[4] W.T. Li, Z.Y. Wang, J.T. Shuai, B.B. Xu, A.Y. Wang, A high oxidation resistance Ti2AlC coating on Zirlo substrates for loss-of-coolant accident conditions, Ceram. Int. 45 (2019) 13912–13922, https://doi.org/10.1016/j.ceramint.2019.04.089.
[5] W. Bao, J. Xue, J.X. Liu, X. Wang, Y. Gu, F. Xu, G.J. Zhang, Coating SiC on Zircaloy-4 by magnetron sputtering at room temperature, J. Alloy, Compd 730 (2017) 81–87, https://doi.org/10.1016/j.jallcom.2017.09.281.
[6] G.M. Son, K.M. Kim, I.C. Bang, Chromia coating with nanofluid deposition and sputtering for accident tolerance, CHF enhancement, Int. J. Heat Mass Tran. 118 (2018) 890–899, https://doi.org/10.1016/j.ijheatmasstransfer.2017.11.060.

[7] K. Jeong-Min, H. Tae-Hyung, P. Joon-Sik, K. Hyun-Gil, Effect of laser surface treatment on the corrosion behavior of FeCrAl-coated TZM alloy, Metals 6 (2016) 29, https://doi.org/10.3390/met6020029.
[8] C. Tang, M. Steinbrueck, M. Stueber, M. Grosse, X. Yu, S. Ulrich, H.J. Seifert, Deposition, characterization and high-temperature steam oxidation behavior of single-phase Ti2AlC-coated Zircaloy-4, Corrosion Sci. 135 (2018) 87–98, https://doi.org/10.1016/j.corsci.2018.02.035.
[9] C. Tang, M. Klimenkov, U. Jaentsch, H. Leiste, M. Rinke, S. Ulrich, M. Steinbrück, H.J. Seifert, M. Stueber, Synthesis and characterization of Ti2AlC coatings by magnetron sputtering from three elemental targets and ex-situ annealing, Surf. Coating. Technol. 309 (2017) 445–455, https://doi.org/10.1016/j.surfcoat.2016.11.090.
[10] P. Sharma, O.P. Pandey, Non-isothermal oxidation kinetics of nano-laminated Cr2AlC MAX phase, J. Alloys Compd. 773 (2019) 872–882, https://doi.org/10.1016/j.jallcom.2018.09.326.
[11] L. Guo, Z. Yan, X.H. Wang, Q.J. He, Ti2AlC MAX phase for resistance against CMAS attack to thermal barrier coatings, Ceram. Int. 45 (2019) 7627–7634, https://doi.org/10.1016/j.ceramint.2019.01.059.
[12] Z. Zhang, D. Lai, S.H. Lim, J. Chai, S. Wang, H. Jin, J. Pan, Isothermal oxidation of the Ti 2 AlC MAX phase coatings deposited by kerosene-fuelled HVOF spray, Corrosion Sci. 138 (2018) 266–274, https://doi.org/10.1016/j.corsci.2018.04.022.
[13] T. Fey, M. Stumpf, A. Chmielarz, P. Colombo, P. Greil, M. Potoczek, Microstructure, thermal conductivity and simulation of elastic modulus of MAX-phase (Ti2AlC) gel-cast foams, J. Eur. Ceram. Soc. 38 (2018) 3424–3432, https://doi.org/10.1016/j.jeurceramsoc.2018.04.012.
[14] H. Yeom, B. Hauch, G.p. Cao, B. Garcia-Diaz, M. Martinez-Rodriguez, H. Colon-Mercado, L. Olson, K. Sridharan, Laser surface annealing and characterization of Ti2AlC plasma vapor deposition coating on zirconium-alloy substrate, Thin Solid Films 615 (2016) 202–209, https://doi.org/10.1016/j.tsf.2016.07.024.
[15] H. Ruan, Z. Wang, L. Wang, L. Sun, H. Peng, P. Ke, A. Wang, Designed Ti/TiN sub-layers suppressing the crack and erosion of TiAlN coatings, Surf. Coating. Technol. 438 (2022), 128419, https://doi.org/10.1016/j.surfcoat.2022.128419.
[16] X. Zuo, D. Zhang, R.D. Chen, P.L. Ke, M. Oden, A.Y. Wang, Spectroscopic investigation on the near-substrate plasma characteristics of chromium HiPIMS in low density discharge mode, Plasma Sources Sci. Technol. 29 (2020), 015013. ARTN01501310.1088/1361-6595/ab5c03.
[17] P.A. Mouche, T. Koyanagi, D. Patel, Y. Katoh, Adhesion, structure, and mechanical properties of Cr HiPIMS and cathodic arc deposited coatings on SiC, Surf. Coating. Technol. 410 (2021), 126939, https://doi.org/10.1016/j.surfcoat.2021.126939.
[18] H.Y. Kyle Quillin, Dabney Tyler, Evan Willing, Kumar Sridharan, Microstructural and nanomechanical studies of PVD Cr coatings on SiC for LWR fuel cladding applications, Surf. Coating. Technol. 441 (2022), 128577, https://doi.org/10.1016/j.surfcoat.2022.128577.
[19] X.C. Han, C. Chen, Y.Q. Tan, W.L. Feng, S.M. Peng, H.B. Zhang, A systematic study of the oxidation behavior of Cr coatings on Zry4 substrates in high temperature steam environment, Corrosion Sci. 174 (2020), 108826, https://doi.org/10.1016/j.corsci.2020.108826.
[20] X. Zuo, R.D. Chen, J.Z. Liu, P.L. Ke, A.Y. Wang, The influence of superimposed DC current on electrical and spectroscopic characteristics of HiPIMS discharge, AIP Adv. 8 (2018), 015132, https://doi.org/10.1063/1.5018037.
[21] X. Zuo, P.L. Ke, R.D. Chen, X.W. Li, M. Oden, A.Y. Wang, Discharge state transition and cathode fall thickness evolution during chromium HiPIMS discharge, Phys. Plasmas 24 (2017), 083507, https://doi.org/10.1063/1.4995482.
[22] A. Anders, A review comparing cathodic arcs and high power impulse magnetron sputtering (HiPIMS), Surf. Coating. Technol. 257 (2014) 308–325, https://doi.org/10.1016/j.surfcoat.2014.08.043.
[23] N.L. Dong, A model for development of orientation of vapour deposits, J. Mater. Sci. 24 (1989) 4375–4378, https://doi.org/10.1007/BF00544515.
[24] Y. Meng, S. Zeng, Z. Teng, X. Han, H. Zhang, Control of the preferential orientation Cr coatings deposited on zircaloy substrates and study of their oxidation behavior, Thin Solid Films 730 (2021), 138699, https://doi.org/10.1016/j.tsf.2021.138699.
[25] H. Yeom, B. Maier, G. Johnson, T. Dabney, M. Lenling, K. Sridharan, High temperature oxidation and microstructural evolution of cold spray chromium coatings on Zircaloy-4 in steam environments, J. Nucl. Mater. 526 (2019), 151737, https://doi.org/10.1016/j.jnucmat.2019.151737.
[26] J.C. Brachet, C. Lorrette, CEA Studies on Advanced Nuclear Fuel Claddings for Enhanced Accident Tolerant LWRs Fuel (LOCA and beyond LOCA Conditions), Fontevraud 8-contribution of Materials Investigations and Operating Experience to Lwrs Safety, Performance and Reliability France, 2015, https://doi.org/10.13140/2.1.5105.6325. Avignon.
[27] X. Peng, M. Li, F. Wang, A novel ultrafine-grained Ni3Al with increased cyclic oxidation resistance, Corrosion Sci. 53 (2011) 1616–1620, https://doi.org/10.1016/j.corsci.2011.01.043.
[28] X. Tan, X. Peng, F. Wang, The effect of grain refinement on the adhesion of an alumina scale on an aluminide coating, Corrosion Sci. 85 (2014) 280–286, https://doi.org/10.1016/j.corsci.2014.04.022.
[29] V.F. Urbanic, T.R. Heidrick, High-temperature oxidation of zircaloy-2 and zircaloy-4 in steam, J. Nucl. Mater. 75 (1978) 251–261, https://doi.org/10.1016/0022-3115(78)90006-5.
[30] Y. Wang, H. Tang, X. Han, W. Feng, X. Zhou, S. Peng, H. Zhang, Oxidation resistance improvement of Zr-4 alloy in 1000 degrees steam environment using ZrO2/FeCrAl bilayer coating, Surf. Coating. Technol. 349 (2018) 807–815, https://doi.org/10.1016/j.surfcoat.2018.05.005.
[31] T.G. Wei, R.Q. Zhang, H.Y. Yang, H. Liu, S.Y. Qiu, Y. Wang, P.N. Du, K. He, X. G. Hu, C. Dong, Microstructure, corrosion resistance and oxidation behavior of Cr-coatings on Zircaloy-4 prepared by vacuum arc plasma deposition, Corrosion Sci. 158 (2019), 108077, https://doi.org/10.1016/j.corsci.2019.06.029.